PCCP

ROYAL SOCIETY OF CHEMISTRY

PAPER

View Article Online
View Journal | View Issue

Cite this: *Phys. Chem. Chem. Phys.*, 2020, **22**, 2130

Reactions of a distonic peroxyl radical anion influenced by SOMO–HOMO conversion: an example of anion-directed channel switching†

Sui So,[a] Benjamin B. Kirk,[b] Uta Wille,[c] Adam J. Trevitt,[b] Stephen J. Blanksby[d] and Gabriel da Silva*[a]

Received 4th November 2019,
Accepted 19th December 2019

DOI: 10.1039/c9cp05989j

rsc.li/pccp

In free radicals the singly occupied molecular orbital (SOMO) typically has the highest energy. Recent examples of distonic radical anions were found, however, to disobey the usual orbital configuration, with the singly occupied molecular orbital buried energetically underneath doubly occupied orbitals. This unusual ordering of electrons, which contradicts the aufbau principle, has been characterized as SOMO–HOMO orbital conversion and is expected to perturb radical anion reactivity by branching toward anion-driven over radical-driven processes. Here, we use ion trap mass spectrometry and *ab initio* calculations to demonstrate that SOMO–HOMO orbital conversion influences the reactivity of a distonic peroxyl radical anion. Experimentally, we generated a distonic radical anion of β-hydroxy glutaric acid, $^{\bullet}CH_2CH(OH)CH_2C(O)O^-$, and investigated its subsequent reaction with O_2 in the gas phase. Theoretical calculations predict that reactions proceed through five isomeric $C_4H_6O_5^{\bullet-}$ intermediates, two of which exhibit SOMO–HOMO conversion. The detected product ions, corresponding to loss of $^{\bullet}OH + CO_2$, $^{\bullet}OH + HCHO$, $HO_2^{\bullet}$, and $HO_2^{\bullet} + CO_2$ from the peroxyl radical, can all be reconciled by the proposed reaction mechanism. Finally, we compare the oxygen recombination reaction of the distonic radical ion to the corresponding neutral radical (*i.e.*, $^{\bullet}CH_2CH(OH)CH_2C(O)OH$). These calculations demonstrate that SOMO–HOMO conversion results in channel switching in the distonic radical anion, suppressing radical-driven mechanisms and promoting pathways that directly involve the anion site.

Introduction

The aufbau principle is conventionally used to explain the arrangement of electrons in atoms and molecules. It postulates that electrons fill orbitals by starting at the lowest available energy level.[1] According to this principle open shell species, or radicals, will have an unpaired electron located in the highest occupied molecular orbital (HOMO), which then becomes a singly occupied molecular orbital (SOMO). However, it was recently discovered that in certain distonic radical anions the electronic arrangement does not conform to the aufbau principle. In these species, the unpaired electron is located in an orbital with a lower energy than other doubly occupied molecular orbitals (DOMOs).[2–4] This peculiar electronic arrangement arises from a stabilising interaction between a remote charge and a radical site. This stabilisation can be classified as coulombic, arising from through-space (as opposed to through-bond) interactions and is non-directional as it does not rely upon dipole-inducing charge separation.[5]

Conventional radical ions have the unpaired electron located at the charge centre or connected through conjugation, and are classically prepared by adding or removing an electron from a neutral closed-shell molecule. However, it was proposed in the early 1970s that radical ions could exist with the charge well-separated from the radical centre.[6,7] These species later came to be termed distonic radical ions,[8] and have now been extensively studied, particularly amongst radical cations.[9,10] The term distonic ions is now widely adopted to describe radical ions in which the unpaired electron and charge are formally assigned to different atoms within a valence bond structure.

The reactivity and stability of distonic radical ions result from contributions from both the radical and ionic functional groups, which exert considerable influence upon each other.

[a] *Department of Chemical Engineering, The University of Melbourne, VIC 3010, Australia. E-mail: gdasilva@unimelb.edu.au*
[b] *School of Chemistry, University of Wollongong, NSW 2522, Australia*
[c] *School of Chemistry and Bio21 Institute, The University of Melbourne, VIC 3010, Australia*
[d] *Central Analytical Research Facility, Institute for Future Environments, Queensland University of Technology, QLD 4001, Australia*

† Electronic supplementary information (ESI) available: Molecular orbitals in the peroxyl radical **W1**. Optimised geometries, vibrational frequencies and moments of inertia of all stationary points at the M06-2X/6-31G(2df,p) level of theory. See DOI: 10.1039/c9cp05989j

These charge-isolated radicals are encountered in many areas, including gas phase radical chemistry,[11,12] liquid phase reaction mechanisms,[13,14] fundamental ion–molecule reaction chemistry,[15–17] and the study of amino acids and peptides.[18,19]

The newly discovered ordering of electrons in the molecular orbitals of distonic radical anions has been termed SOMO–HOMO orbital conversion.[5,20] This phenomenon is particularly prevalent when the molecule consists of a sufficiently stabilised radical (*e.g.*, peroxyl, aminoxyl, aminyl) contributing the SOMO, and a negative charge which is localised on a conjugate base of a weak acid (*e.g.*, carboxylate, phosphate, sulfate, alkoxide).[20] As a consequence of the through-space stabilisation, the SOMO of the radical ion is no longer the HOMO and is submerged to a lower energy level. The stabilising effect that accompanies SOMO–HOMO conversion can act as a protective mechanism for carbon-centred radicals,[20] and is proposed to have potential application in pH-switchable compounds for organic synthesis and nitroxide-mediated polymerisation.[5]

The current study investigates the gas-phase reaction of the β-hydroxyglutaric acid radical anion $^{\bullet}CH_2CH(OH)CH_2C(O)O^-$ with O_2 both experimentally and theoretically and extends from our recent study of the oxidation chemistry of a methyl-hydroxyglutaric acid radical anion.[11] The radical centre in $^{\bullet}CH_2CH(OH)CH_2C(O)O^-$ is located on the terminal carbon, remote from the negatively charged carboxylate terminus. Reaction with O_2 proceeds *via* the distonic peroxyl radical anion $^{\bullet}O_2CH_2CH(OH)CH_2C(O)O^-$, which is subject to SOMO–HOMO conversion (*vide infra*). Theoretical calculations reveal that the anionic site influences the reaction chemistry of the radical anion through a variety of mechanisms, which is witnessed in the experimentally detected dissociation products of the peroxyl radical. This represents the first time that SOMO–HOMO conversion has been shown to influence the product distribution of a bimolecular gas-phase reaction.

Results and discussion

Orbital conversion

Recent studies have revealed that SOMO–HOMO orbital conversion is commonly encountered in distonic radical anions.[5,14,20] The carboxylato-peroxyl radical anion examined in this work, $^{\bullet}O_2CH_2CH(OH)CH_2C(O)O^-$, which is subject to SOMO–HOMO orbital conversion (*vide infra*), is shown in Scheme 1.

Fig. 1 shows the electronic arrangement and selected molecular orbitals of the distonic radical anion $^{\bullet}O_2CH_2CH(OH)CH_2C(O)O^-$

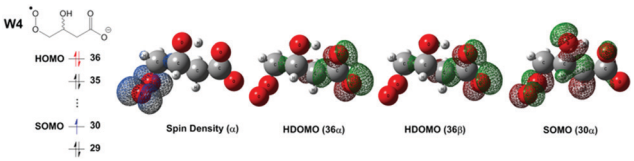

Fig. 1 Electronic arrangement and molecular orbital configurations of the distonic radical anion $^{\bullet}O_2CH_2CH(OH)CH_2C(O)O^-$ (**W1**). The geometry is optimised at the M06-2X/aug-cc-pVTZ level of theory. The α-electron spin density, highest doubly occupied molecular orbital (HDOMO) and singly occupied molecular orbital (SOMO) are also indicated. The numbering of molecular orbitals is assigned in order of increasing energy.

(**W1**), with Fig. S1 of the ESI† illustrating the first 9 alpha (α) and 8 beta (β) orbitals. The electrons of the negatively charged carboxylate group occupy the HOMO (red), whereas the SOMO with the unpaired electron of the peroxyl radical moiety (blue) is submerged to become the seventh highest energy molecular orbital. This results in the unconventional electronic arrangement where the SOMO is less energetic than the HOMO, indicating SOMO–HOMO orbital conversion of the distonic radical anion **W1**. The energy difference between HOMO and SOMO is calculated to be 0.12 eV (2.8 kcal mol^{-1}).

Fig. S1 (ESI†) reveals that orbitals 36 to 33, and orbitals 29 and below, are all very well-described as DOMOs, in terms of both energy and structure of the α- and β-electron components. Orbitals 30α–32α and 31β–32β, however, cannot be well-organized into DOMOs but among these 30α stands alone with no β-orbital of near-equivalent energy. We see that the SOMO is responsible for the bulk of the unpaired α-electron density, yet it also contributes significant electron density at the hydroxyl group, which is largely cancelled by terms from 31β. As a result, DOMO 31 is significantly spin polarized, which in turn perturbs DOMO 32 before these orbital conversion effects die out.

The α-electron spin density plot in Fig. 1 supports our assertion that the unpaired electron is predominantly localised on the peroxyl moiety and unrelated to the HOMO. In order to confirm the orbital assignments in **W1**, comparisons have been made to two related molecules. Referring to Fig. 2, these are: (a) the corresponding closed-shell hydroperoxide anion formed by adding a hydrogen atom ($HO_2CH_2CH(OH)CH_2C(O)O^-$), and (b) the neutral radical formed by adding a proton to the carboxylate moiety ($^{\bullet}O_2CH_2CH(OH)CH_2C(O)OH$). Comparing the HOMO structure in the closed-shell anion to the highest doubly occupied molecular orbital (HDOMO) in **W1** confirms that the electrons in these orbitals are indeed associated with

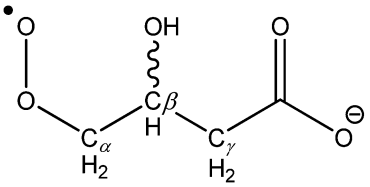

Scheme 1 Structure of the β-hydroxyperoxyl distonic radical anion $^{\bullet}O_2CH_2CH(OH)CH_2C(O)O^-$ (**W1**). All calculations are for the *R* enantiomer, although the precursor used in the experiments is achiral.

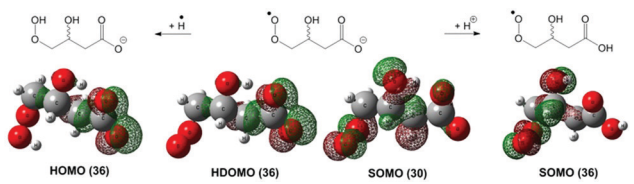

Fig. 2 HOMO and SOMO molecular orbitals of the distonic radical anion $^{\bullet}O_2CH_2CH(OH)CH_2C(O)O^-$ (**W1**), together with the corresponding orbitals in the closed-shell anion after adding a hydrogen atom and the neutral radical after adding a proton.

the carboxylate moiety and not the radical centre. Considering the neutral radical, the highest-energy orbital is found to be the SOMO arising from the peroxyl radical moiety, in accordance with the aufbau principle. Comparing the SOMO in **W1** (30α) and the neutral radical (36α) provides further confirmation of our orbital assignments, demonstrating that these two open-shell MOs arise from a similar peroxyl radical functionality. On the whole, these findings clearly support the electronic configuration described in Fig. 1, where the peroxyl radical **W1** exhibits SOMO–HOMO conversion. Subsequently, the reaction chemistry of this peroxyl radical has been studied.

Reaction of $^{\bullet}CH_2CH(OH)CH_2C(O)O^-$ + O_2

Mass spectrometry. The distonic radical anion $^{\bullet}O_2CH_2CH(OH)CH_2C(O)O^-$ (**W1**) is the postulated key intermediate in the reaction of the β-hydroxyalkyl radical anion $^{\bullet}CH_2CH(OH)CH_2C(O)O^-$ with O_2. The reactant $^{\bullet}CH_2CH(OH)CH_2C(O)O^-$ has been synthesised and isolated in the gas phase using electrospray ionisation (ESI) and ion-trap mass spectrometry, as shown in Scheme 2. The dicarboxylate dianion at *m*/*z* 73 is produced by subjecting a methanolic solution of 3-hydroxyglutaric acid to electrospray ionisation, followed by irradiation of the mass-selected *m*/*z* 73 dianion population with a 266 nm laser pulse. As a result of photo-detachment and decarboxylation, the target radical anion at *m*/*z* 102 is generated.

Fig. 3 illustrates the mass spectra of (a) isolation of the 3-hydroxyglutaric acid dianion, and (b) photo-detachment of the isolated dianion. For details see Experimental methods.

Isolation of the *m*/*z* 102 radical anion $^{\bullet}CH_2CH(OH)CH_2C(O)O^-$ for 5 s in the presence of O_2 results in the mass spectrum shown in Fig. 4. There are only four product ions observed in appreciable yields; a major channel at *m*/*z* 73 with a loss of 29 Da [$R^{\bullet-} + O_2 - {}^{\bullet}CHO_3$], and minor channels at *m*/*z* 57, 87, and 101 corresponding to respective loss of 45 Da [$R^{\bullet-} + O_2 - CHO_4^{\bullet}$], 15 Da [$R^{\bullet-} + O_2 - CH_3O_2^{\bullet}$], and 1 Da [$R^{\bullet-} + O_2 - HO_2^{\bullet}$]. These four reaction channels can be rationalised in terms of fragmentation of the $^{\bullet}O_2CH_2CH(OH)CH_2C(O)O^-$ peroxyl radical intermediate. The major product ion at *m*/*z* 73 is attributed to loss of $^{\bullet}OH$ and CO_2, and the other product ions are proposed to arise from loss of $HO_2^{\bullet}$ and CO_2 (*m*/*z* 57), $^{\bullet}OH$ and HCHO (*m*/*z* 87) and $^{\bullet}HO_2$ (*m*/*z* 101). A species with a mass-to-charge ratio of the stabilised peroxyl radical at *m*/*z* 134 was not detected. There are very low abundant and poorly resolved ions observed in the range of *m*/*z* 116–119 which might be indicative of minor reaction pathways resulting in fragile reaction products that do not survive mass analysis.[21] These features are not discussed further here.

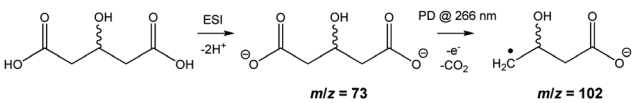

Scheme 2 Gas phase synthesis of the β-hydroxyalkyl radical anion $^{\bullet}CH_2CH(OH)CH_2C(O)O^-$ *via* electrospray ionisation of 3-hydroxyglutaric acid to yield the dianion with subsequent UV photo-detachment-dissociation (PD) to produce the target radical anion at *m*/*z* 102.

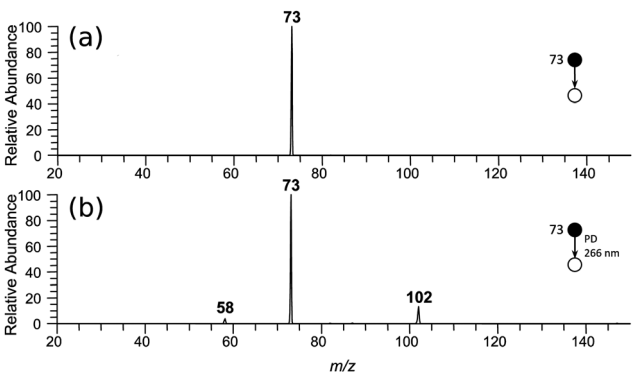

Fig. 3 (a) Isolation of the 3-hydroxyglutaric acid dianion (*m*/*z* 73) in the gas phase. (b) Photodetachment-dissociation of *m*/*z* 73.

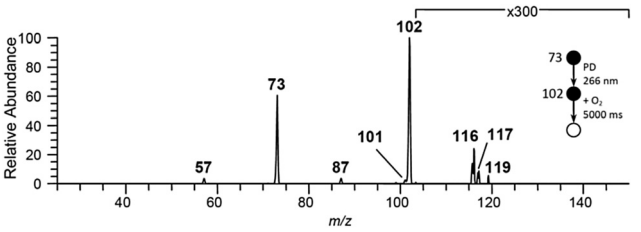

Fig. 4 Mass spectrum resulting from the $^{\bullet}CH_2CH(OH)CH_2C(O)O^-$ (*m*/*z* 102) radical anion reaction with O_2 after 5 s of reaction time. The *m*/*z* 102 ion was synthesised in the gas phase following Scheme 2 and was isolated in the presence of O_2.

The $^{\bullet}CH_2CH(OH)CH_2C(O)O^-$ + O_2 reaction is observed to follow pseudo first-order kinetics. The measured first-order rate coefficient (k_1) is 5.3 ± 0.2 s^{-1} with the concentration of O_2 maintained at (1.3 ± 0.1) × 10^{11} molecule cm^{-3}. The second-order rate coefficient (k_2) of the $^{\bullet}CH_2CH(OH)CH_2C(O)O^-$ + O_2 reaction can, therefore, be determined as (4.0 ± 0.2) × 10^{-11} cm^3 $molecule^{-1}$ s^{-1}. Using an ion–molecule collision rate coefficient (k_{coll}) of 6.0 × 10^{-10} cm^3 $molecule^{-1}$ s^{-1}, the reaction efficiency (ϕ) is calculated to be 6.6%; typical of alkyl radical anion recombination with O_2.[11]

Further experiments using $^{18}O_2$ and the deuterated isotopologue $^{\bullet}CH_2CH(OD)CH_2C(O)O^-$ (*m*/*z* 103) were carried out to aid product ion assignments and gain further knowledge of the reaction mechanism. The reaction of $^{\bullet}CH_2CH(OH)CH_2C(O)O^-$ with $^{18}O_2$ reveals that the product formerly detected at *m*/*z* 73 now appears as two distinct isotopologues at *m*/*z* 73 and 75, whereas the other product ions at *m*/*z* 57, 87 and 101 did not present with splitting of the signals. During the experiment, both $^{18}O_2$ and $^{16}O_2$ are present, and the product ion at *m*/*z* 73 is attributed to the reaction with background oxygen. The appearance of a product ion at *m*/*z* 75, however, suggests that one of the oxygen atoms from $^{18}O_2$ is retained in this product ion. Conversely, the *m*/*z* 87 and 101 products appear to expel both of the $^{18}O_2$ oxygen atoms present in the transient peroxyl radical. The deuterated isotopologue $^{\bullet}CH_2CH(OD)CH_2C(O)O^-$ (*m*/*z* 103), was prepared by electrospray of the precursor from d_1-methanol. This results in the exchange of the hydroxyl group in the radical anion to deuterated hydroxyl group (OD). When this isotopologue (*m*/*z* 103) was isolated in the presence of O_2,

isotopic splitting of the signals is observed for both the product ions originally appearing at *m*/*z* 73 and 87, now appearing at 73/74 and 87/88 respectively. This advocates that both products may either incorporate or expel the hydroxyl deuterium; an indication of hydrogen transfer and scrambling through the dissociation pathways. The product ions originally observed at *m*/*z* 57 and 102, however, are now shifted to *m*/*z* 58 and 103, indicating that these pathways do not involve the OH group.

Reaction mechanism. The possible mechanism of the reaction $^{\bullet}CH_2CH(OH)CH_2C(O)O^- + O_2$ is shown in Scheme 3. The initial peroxyl radical and its $C_4H_6O_5^{\bullet -}$ isomers are identified within the box in the scheme, and their electronic configurations are discussed below. The geometries of the isomeric wells, dissociated product ions, and transition states are illustrated in Fig. S2 of the ESI.† Optimised geometries, vibrational frequencies and moments of inertia of all the wells and transition states at the M06-2X/6-31G(2df,p) level of theory are provided in the ESI.† The energy calculations are in relatively good agreement between the two model chemistries with a mean absolute deviation between G4 and M06-2X of 1.5 kcal mol^{-1}.

The $^{\bullet}CH_2CH(OH)CH_2C(O)O^- + O_2$ reaction begins with barrierless recombination of O_2 and the radical anion. This exothermic reaction generates the peroxyl radical anion **W1** which is 38.5 kcal mol^{-1} lower than the reactants; this chemical activation provides **W1** with appreciable excess vibrational energy that fuels subsequent rapid dissociation. The β-hydroxyperoxyl radical anion **W1** may then undergo unimolecular isomerisation to yield the other $C_4H_6O_5^{\bullet -}$ isomers **W2**, **W3**, **W4** and **W5**. These rearrangements involve 1,4-hydrogen shift from the β-methylene group (C_β abstraction) to yield **W5**, 1,5-hydrogen shifts from the γ-methylene group (C_γ abstraction) to yield **W2** and from the β-hydroxyl group (OH abstraction) to yield **W7**. The nomenclature of the peroxyl radical anion **W1** is given in Scheme 1.

Fig. 5 depicts the potential energy surface for the lowest-energy (C_β-abstraction) reaction channel in the $^{\bullet}CH_2CH(OH)CH_2C(O)O^- + O_2$ system, which leads to product ions of *m*/*z* 58.

The C_β-abstraction pathway is expected to dominate the transmission of the overall reaction flux, as **TS1** is the lowest energy transition state connected to **W1**. The subsequent fragmentations then proceed with barriers (**TS2** and **TS10**) that are lower than **TS1**. As a result, the corresponding product set $HOCH_2C(O^-)CH_2$ + $^{\bullet}OH$ + CO_2 is predicted to be the major product of the $^{\bullet}CH_2CH(OH)CH_2C(O)O^- + O_2$ reaction. The C_β-abstraction proceeds by 1,4-hydrogen shift, through **TS1** producing the hydroperoxide radical anion **W2** with a reaction barrier that is 20.5 kcal mol^{-1} below the entrance energy. **W2** can further perform a proton transfer from the β-hydroxyl group to the carboxylate moiety, with a barrier of only 4.6 kcal mol^{-1} (**TS2**). This forms the alkoxide radical anion **W3** which is 1.1 kcal mol^{-1} higher than **W2**. Expulsion of $^{\bullet}OH$ through **TS10** (27.0 kcal mol^{-1} lower than the initial reactants) generates $HOCH_2C(O)CH_2C(O)O^-$, followed by barrierless dissociation to form the product set

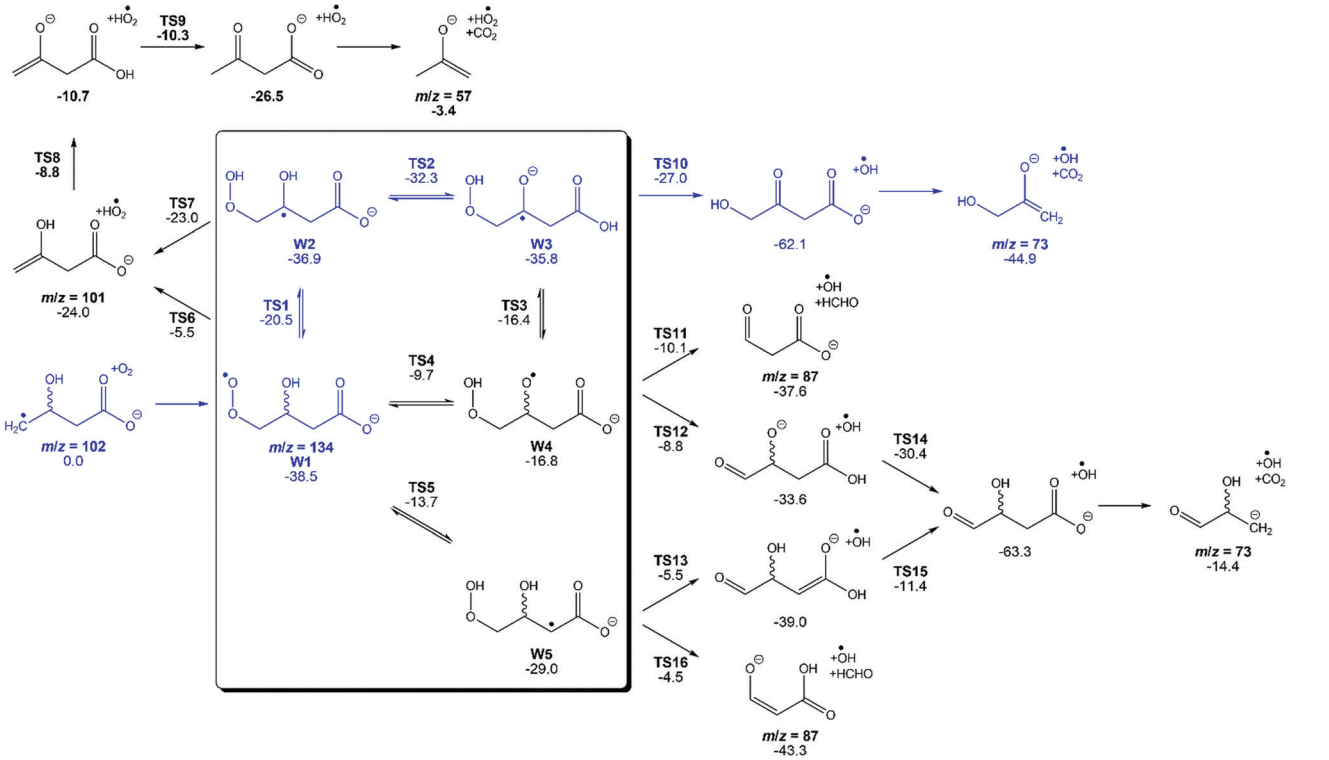

Scheme 3 Mechanism of radical anion $^{\bullet}CH_2CH(OH)CH_2C(O)O^- + O_2$ reaction. Energies at 0 K with zero-point energy (E_0 + ZPE) are shown using the G4 composite method in units of kcal mol^{-1}. The mass to charge ratios (*m*/*z*) are indicated for detected product ions. The intermediate wells boxed in the scheme are $C_4H_6O_5^{\bullet -}$ isomers. The blue reaction pathway is identified as the lowest energy channel (see Fig. 5 for more detail), consistent with the experimental observations.

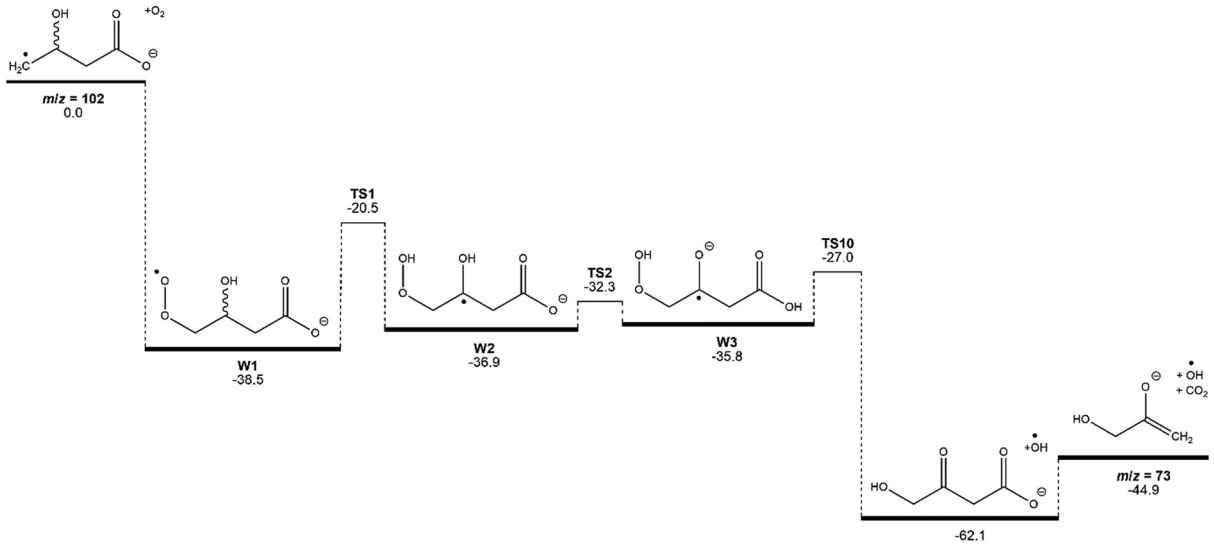

Fig. 5 *Ab initio* potential energy surface of the major reaction channel in the radical anion $^{\bullet}CH_2CH(OH)CH_2C(O)O^-$ + O_2 reaction system. G4 energies at 0 K with zero-point energy (E_0 + ZPE) are shown in units of kcal mol^{-1}. The mass to charge ratio (*m*/*z*) are indicated for product ions.

$HOCH_2C(O^-)CH_2$ + $^{\bullet}OH$ + CO_2. As can be seen in Scheme 3, the β-hydroxyperoxyl radical **W1** can alternatively undergo a 1,5-hydrogen shift through **TS4** with a barrier of 28.8 kcal mol^{-1} *via* the OH abstraction channel, ultimately yielding the product sets $OCHCH_2C(O)O^-$ + $^{\bullet}OH$ + HCHO and $OCHCH(OH)CH_2^-$ + $^{\bullet}OH$ + CO_2 by unimolecular decomposition. Furthermore, **W1** can also proceed *via* the C_γ-abstraction channel, performing a 1,5-hydrogen shift through a barrier of 24.8 kcal mol^{-1} (**TS5**). The corresponding product sets after fragmentation and decarboxylation for this pathway are $OCHCHC(O^-)OH$ + $^{\bullet}OH$ + HCHO and $OCHCH(OH)CH_2^-$ + $^{\bullet}OH$ + CO_2. It is also seen that, apart from isomerisation, **W1** also decomposes to form product ion $CH_2C(OH)CH_2C(O)O^-$ through concerted $HO_2^{\bullet}$ elimination[22–24] *via* **TS6**, which is 5.5 kcal mol^{-1} below the entrance energy. Moreover, **W5** can also undergo fragmentation through **TS7** to form $CH_2C(OH)CH_2C(O)O^-$ + $HO_2^{\bullet}$. This latter concerted $HO_2^{\bullet}$ elimination pathway through **TS7** has a reaction barrier which is 17.5 kcal mol^{-1} lower than the former channel through **TS6**. Finally, $CH_2C(OH)CH_2C(O)O^-$ can then undergo a series of hydrogen abstraction reactions through **TS8** and **TS9**, ultimately producing $H_3C(O^-)CH_2$ + $HO_2^{\bullet}$ + CO_2. However, this pathway is predicted to be of little significance as the energy of $H_3C(O^-)CH_2$ + $HO_2^{\bullet}$ + CO_2 is just 3.4 kcal mol^{-1} below the entrance channel.

The reaction mechanism proposed in Scheme 3 is consistent with the experimental findings discussed above including the isotope labelling studies. For the $^{18}O_2$ experiments, one of the oxygen atoms in the $^{18}O_2$ is retained in the product ion through C_β-abstraction, but both oxygen atoms in $^{18}O_2$ leave in $^{\bullet}OH$ and CO_2 after decomposition in the OH and C_γ-abstraction pathways. For the deuterated compound, splitting of the signal across two isotopologues is observed for the product ions arising from loss of $^{\bullet}OH/^{\bullet}OD$ followed by formaldehyde. The C_β- and C_γ-abstraction channels retain deuterium in $HOCH_2C(O^-)CH_2$ and $OCHCH(OH)CH_2^-$, but the OH-abstraction pathway expels deuterium as $^{\bullet}OD$. This explains the observation of peaks at *m*/*z* 73 and 74. Similar trends are also observed for the other product ions from elimination of $^{\bullet}OH$ followed by decarboxylation, where the OH abstraction channel leads to the product ion at *m*/*z* 87 and the C_γ-abstraction pathway results in formation of the product ion at *m*/*z* 88. However, only one signal is observed for the product ions attributed to the elimination of $^{\bullet}HO_2$ followed by decarboxylation. The deuterium is retained in the radical anion after the elimination of $^{\bullet}HO_2$ (shifting the ion from *m*/*z* 101 to 102) and in the subsequent decarboxylation to yield a product ion *m*/*z* 58.

Radical anion stability

As shown in Scheme 3, the distonic radical anion **W1** can transform to a suite of different $C_4H_6O_5^{\bullet-}$ isomers, which may or may not exhibit SOMO–HOMO conversion. Fig. 6 illustrates the electronic arrangement and molecular orbital configurations of these $C_4H_6O_5^{\bullet-}$ isomers, *i.e.*, (a) **W2**, (b) **W3**, (c) **W4** and (d) **W5**. SOMO–HOMO conversion is observed for **W4**, where the SOMO arising from the localised oxyl radical site has been buried below the HOMO corresponding to the carboxylate moiety, to become the sixth highest MO (MO 31). This finding is consistent with past predictions for alkoxyl radical moieties in comparable distonic radical anions.[15]

We will consider first the $C_4H_6O_5^{\bullet-}$ isomers, **W2**, **W3** and **W5** that exhibit traditional aufbau orbital configurations. The radical site is localised at the β-carbon in **W2**, which is the same as in a conventional distonic radical anion. While formally the structures of **W3** and **W5** localise the charge and unpaired electron on different atoms, both species are cross-conjugated affording direct resonance stabilization and a resulting canonical electronic configuration. The negative charge is not directly coupled with the radical site in **W3** and **W5**, and as such they are not distonic radical ions. However, the resonance in **W3** and **W5** stabilises the carboxylate group by delocalising the negative charge.

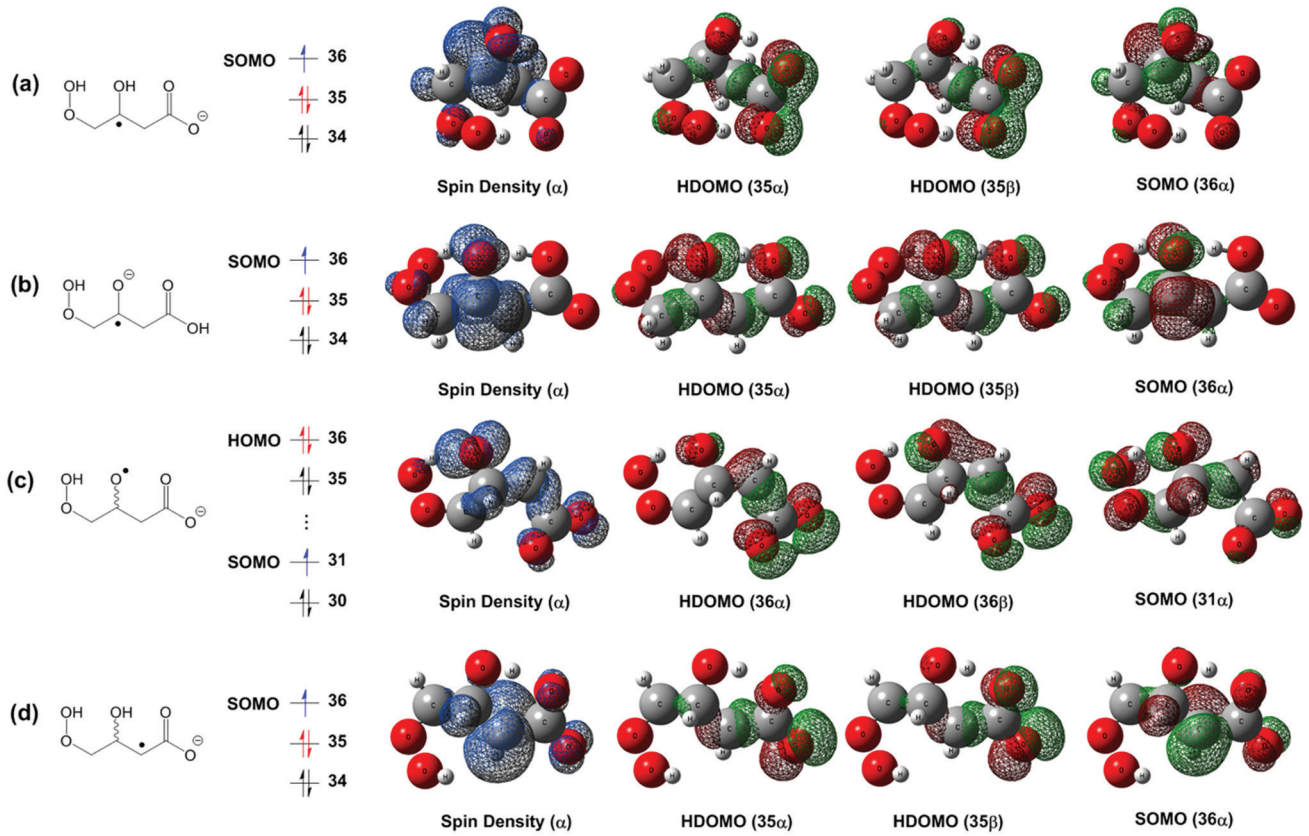

Fig. 6 Electronic arrangement and molecular orbital configurations of the radical anions for (a) **W2**, (b) **W3**, (c) **W4** and (d) **W5**. Geometries are optimised at the M06-2X/aug-cc-pVTZ level of theory. The α electron spin density, highest doubly occupied molecular orbital (HDOMO) and singly occupied molecular orbital (SOMO) are also indicated. Molecular orbitals are numbered in order of increasing energy.

As with the parent peroxyl radical anion **W1**, the electronic configurations of the $C_4H_6O_5^{\bullet-}$ isomers have been further examined through comparison to their analogous closed-shell anions and neutral radicals formed through respective hydrogen atom addition and protonation. Fig. 7 demonstrates the HOMO in the closed-shell anions, the HDOMO and SOMO in the radical anions and the SOMO in the neutral radicals. It shows that the HOMOs and HDOMOs are comparable to each other, and that the SOMOs are also similar.

Although the orbitals for the $C_4H_6O_5^{\bullet-}$ isomers can be assigned with confidence, assignment in the case of the reactant $^{\bullet}CH_2CH(OH)CH_2C(O)O^-$ is somewhat ambiguous (Fig. 8). This is likely due to the lower polarizability of the carbon-centred radical compared to the peroxyl moiety in **W1**.[14,15] The two viable electronic assignments for $^{\bullet}CH_2CH(OH)CH_2C(O)O^-$ are shown in Fig. 9. The aufbau configuration provides the SOMO (28α) that best matches the unpaired α spin density but results in the highest two DOMOs being significantly spin polarized (0.013 and 0.005 eV). In the SOMO–HOMO converted arrangement the SOMO does not account for the majority of the unpaired electron density and the HOMO is highly spin polarized (0.020 eV), but the intervening two DOMOs are better matched in terms of energy and structure than the corresponding aufbau assignments. We therefore argue that $^{\bullet}CH_2CH(OH)CH_2C(O)O^-$ is not a fully developed example of SOMO–HOMO conversion, and that any additional stability conferred to the SOMO in this radical anion is effectively cancelled out by the instability arising from orbital spin polarization. Nonetheless we can still consider this species as having undergone SOMO–HOMO conversion.

Fig. 10 illustrates the orbital configuration of two molecules similar to $^{\bullet}CH_2CH(OH)CH_2C(O)O^-$, which are the corresponding closed-shell anion after adding a hydrogen atom ($CH_3CH(OH)CH_2C(O)O^-$) and the neutral radical after adding a proton ($^{\bullet}CH_2CH(OH)CH_2C(O)OH$). Contrary to the same analysis for the hydroxyperoxyl radical anion **W1**, there are discrepancies in the location of electron density in the HDOMO in $^{\bullet}CH_2CH(OH)CH_2C(O)O^-$ and the HOMO in the corresponding closed-shell anion. Differences are also observed between the SOMOs in $^{\bullet}CH_2CH(OH)CH_2C(O)O^-$ and its neutral radical analogue. The closed-shell anion does not possess a SOMO and the HOMO is attributed to the doubly occupied MO arising predominantly from the carboxylate group of the molecule. On the other hand, the neutral radical carries a SOMO, which is also the HOMO of the molecule corresponding to the methylene radical site. In this case, the HDOMO and SOMO of $^{\bullet}CH_2CH(OH)CH_2C(O)O^-$ are influenced by both the carboxylate group and the methylene radical site, showing that the unpaired electron is likely to appear at the charge and radical site. This assignment is also consistent with the equivocal nature of $^{\bullet}CH_2CH(OH)CH_2C(O)O^-$.

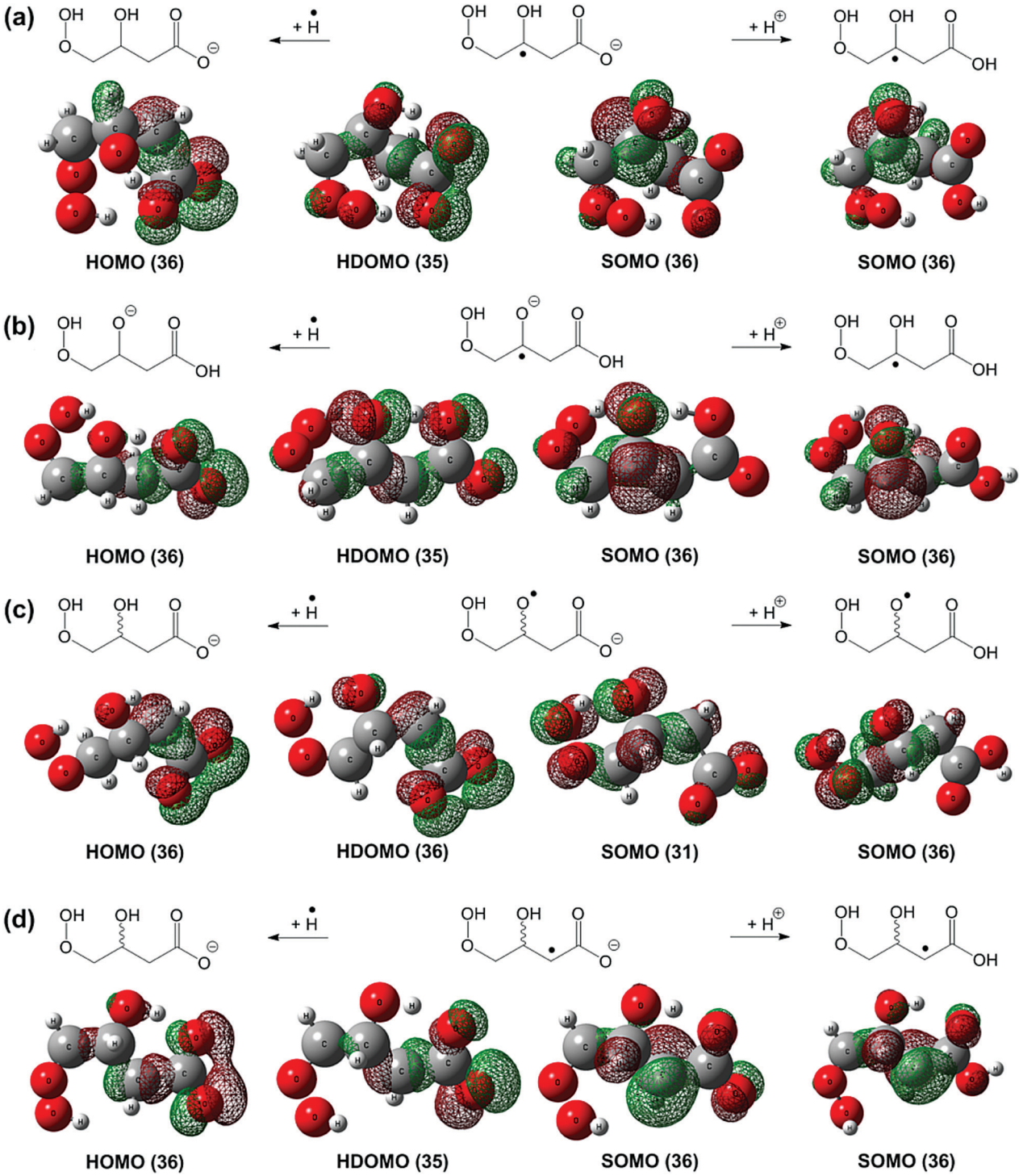

Fig. 7 The molecular orbital configurations of (a) **W2**, (b) **W3**, (c) **W4** and (d) **W5**, together with the corresponding orbitals in the closed-shell anions after adding a hydrogen atom and the neutral radicals after adding a proton.

The SOMO–HOMO converted radical anions discussed above may potentially exhibit different degrees of stabilisation, and we now attempt to quantify the change in stability between these radical anions and their analogous neutral radicals. To do this we use the bond dissociation energy (BDE), which is a common measure of radical stability,[14,15] for the dissociation $Y\text{–}CH_3 \rightarrow Y^{\bullet} + {}^{\bullet}CH_3$, where $Y^{\bullet}$ are the anionic and protonated neutral radicals which exhibit SOMO–HOMO conversion (*i.e.*, **W1**, **W4** and ${}^{\bullet}CH_2CH(OH)CH_2C(O)O^{-}$). The BDEs are calculated at the M062X/aug-cc-pVTZ level of theory, and the change in stability of the radicals upon protonation is then estimated by the difference in BDE between the neutral and anionic species.

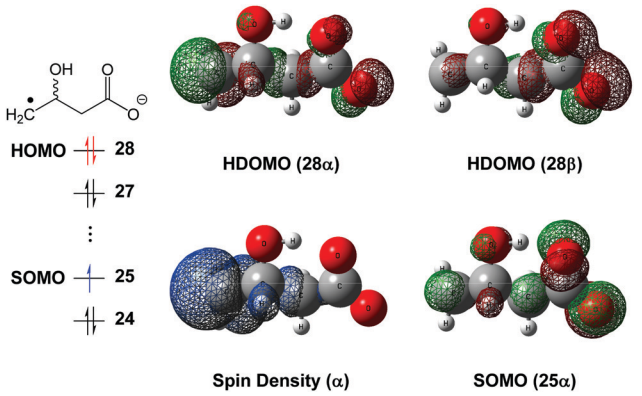

Fig. 8 The electronic arrangement and molecular orbital configurations of the distonic radical anion $^{\bullet}CH_2CH(OH)CH_2C(O)O^{-}$. The geometry is optimised at the M06-2X/aug-cc-pVTZ level of theory. The α electron spin density, highest doubly occupied molecular orbital (HDOMO) and singly occupied molecular orbital (SOMO) are also indicated. Molecular orbitals are numbered in order of increasing energy.

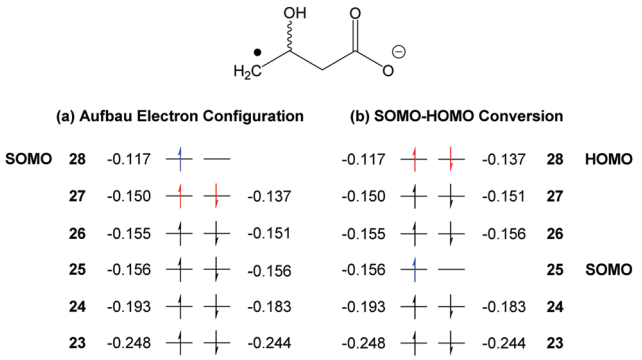

Fig. 9 Two proposed electron configurations for the radical anion $^{\bullet}CH_2CH(OH)CH_2C(O)O^{-}$, (a) following the aufbau principle, and (b) exhibiting SOMO–HOMO conversion. The energy of the molecular orbitals (in eV) is calculated at the M06-2X/aug-cc-pVTZ level of theory.

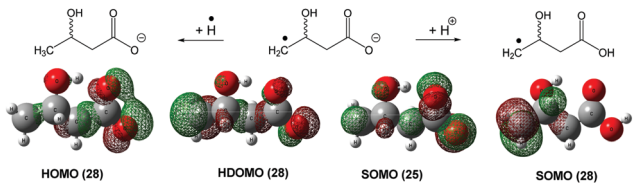

Fig. 10 The molecular orbital configurations of the distonic radical anion $^{\bullet}CH_2CH(OH)CH_2C(O)O^{-}$, together with the molecular orbital configuration of the corresponding closed-shell anion $CH_3CH(OH)CH_2C(O)O^{-}$ after adding a hydrogen atom and neutral radical $^{\bullet}CH_2CH(OH)CH_2C(O)OH$ after adding a proton.

Although not entirely due to HOMO–SOMO conversion, the decrease in BDE of the radical anions *versus* their protonated analogues provides a good indication of the stabilising effect. The data, given in Table 1, reveal that the stability gained by the interaction between the charge and radical site in **W1** and **W4** is 5.5 ± 0.1 kcal mol^{-1}, whereas, the change in stability of $^{\bullet}CH_2CH(OH)CH_2C(O)O^{-}$ is considerably less, at *ca.* 0.8 kcal mol^{-1}. These calculations further support that **W1** and **W4** exhibit appreciable through-space stabilisation between the charge and radical site, and that $^{\bullet}CH_2CH(OH)CH_2C(O)O^{-}$ shows characteristics of both conventional aufbau and orbital-converted electron configurations.

Comparison of radical anion and neutral radical reactivity

Radical anions may be subject to a range of stabilisation mechanisms when compared to their analogous neutral radicals. They may also undergo reactions without contributions from the radical site, such as proton transfer. It is therefore plausible that deprotonation of a radical species may result in channel switching between the analogous pathways on the radical anion and neutral radical surfaces.

Energies of selected wells and transition states are presented in Fig. 11 for the anionic and the protonated neutral radical systems studied here.

There are four reactions with significant observable differences between the radical anion and the neutral radical reaction system, namely (i) barrierless O_2 addition, (ii) H abstraction from the γ-carbon (**TS5**), (iii) H abstraction from the β-hydroxyl group (**TS4**), and (iv) H abstraction from the β-carbon (**TS1**), and these are discussed in turn below. To aid in the discussion, the key transition states for the radical anion case are depicted in Scheme 4, along with curved arrow diagrams indicating the bond breaking and forming processes. Significantly, the overall effect is that, once the β-hydroxyperoxyl radical **W1** is formed, facile H abstraction from the β-carbon through **TS1** (red pathway) is the expected dominant reaction pathway with the lowest energy barrier for the radical anion. On the other hand, this pathway is supressed in the neutral radical, where H abstraction from the β-hydroxyl moiety through **TS4** (green pathway) has the lowest reaction barrier.

Barrierless O_2 addition

The barrierless addition of O_2 to $^{\bullet}CH_2CH(OH)CH_2C(O)O^{-}$ of the radical anion analogue is 5.1 kcal mol^{-1} more exothermic than the same reaction of the neutral radical analogue. This discrepancy is attributed to spin polarisation hindering long-range stabilisation of $^{\bullet}CH_2CH(OH)CH_2C(O)O^{-}$. This loss of stability in the reactant, which is present in the product, results in a greater exothermicity in the radical anion system than in

Table 1 Calculated bond dissociation energy (BDE) of Y–CH_3, where Y$^{\bullet}$ are the radicals which exhibit SOMO–HOMO conversion, in both the radical anion and neutral radical form, in the $^{\bullet}CH_2CH(OH)CH_2C(O)O^{-}$ + O_2 reaction

	Radical anion BDE (kcal mol^{-1})	Neutral radical BDE (kcal mol^{-1})	BDE change (kcal mol^{-1})
W1	61.3	66.7	5.4
W4	76.4	82.0	5.6
$^{\bullet}CH_2CH(OH)CH_2C(O)O^{-}$	87.7	88.5	0.8

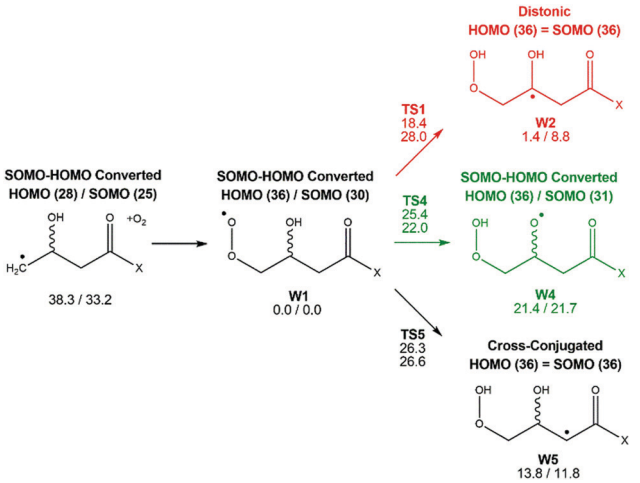

Fig. 11 Selected wells and transition states of the $^{\bullet}CH_2CH(OH)CH_2C(O)X + O_2$ reaction (where X = O^- or OH). Energies at 0 K with zero-point energy (E_0 + ZPE) are shown in units of kcal mol^{-1} at M06-2X/aug-cc-pVTZ level of theory. Energies for the radical anion system (X = O^-) are listed first, followed by the neutral radical system (X = OH). The red pathway is the lowest-energy channel in the radical anion system. The green pathway is the lowest-energy channel in the neutral radical system.

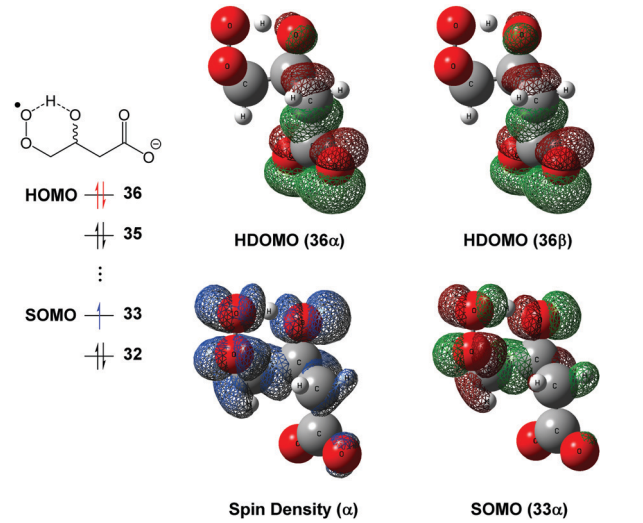

Fig. 12 The electronic arrangement and molecular orbital configurations of **TS4**. The geometry is optimised at the M06-2X/aug-cc-pVTZ level of theory. The α electron spin density, highest doubly occupied molecular orbital (HDOMO), and singly occupied molecular orbital (SOMO) are also indicated. Molecular orbitals are numbered in order of increasing energy.

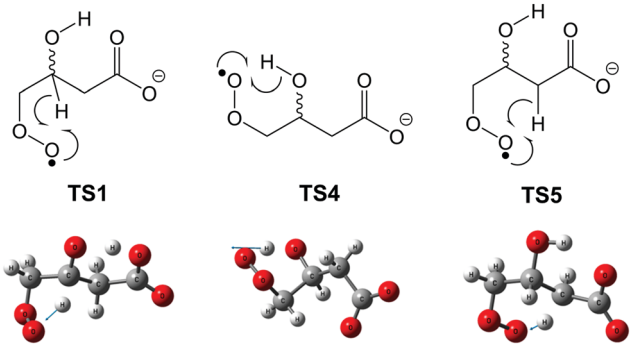

Scheme 4 Optimized structures of **TS1**, **TS4**, and **TS5**, with corresponding electronic rearrangements in **W1** according to the curved arrow formalism.

the analogous neutral case. This finding is consistent with the recent data from Williams *et al.*[25]

H abstraction from the γ-carbon

The energy of **W5** relative to **W1** is about 2 kcal mol^{-1} higher in the radical anion compared to the protonated neutral. Even though the radical anion **W5** does not exhibit SOMO–HOMO conversion, it is stabilised by cross-conjugation of the radical site and the carboxylate group, resulting in a similar energy difference across this reaction (and in **TS5**) for the anionic and neutral systems.

H abstraction from the β-hydroxyl group

The energy difference of **W4** relative to **W1** is negligible, due to the fact that both **W1** and **W4** exhibit SOMO–HOMO conversion and similar degrees of added stability (*cf.* Table 1). There is also a slight difference in the **TS4** reaction barrier between radical anion and neutral radical; **TS4** is the transition state of the H abstraction from the β-hydroxyl moiety to the peroxyl group, producing **W4** from **W1**. Referring to Fig. 1 and 6, the SOMO of **W1** and **W4** is assigned to MO 30 and MO 31 respectively, with MO 36 being the HOMO in both molecules. Fig. 12 provides the electron configuration of **TS4**. The SOMO of **TS4** is assigned to MO 33, such that the effect of SOMO–HOMO conversion is not as apparent as in the reactants and products, leading to a lesser degree of stabilisation of **TS4**. Therefore, the reaction barrier of **TS4** is slightly higher in the radical anion form compared to the neutral radical, due to the temporary loss of stability transforming from **W1** to **W4**.

H abstraction from the β-carbon

There is a large energy difference between the anionic and neutral radical system for **W2** relative to **W1**, due to **W2** being a conventional distonic radical anion. This leads to the loss of stability associated with the HOMO–SOMO conversion in **W1**. Therefore, the H abstraction from the β-carbon through **TS1** is less endothermic in the radical anion system, due to the extra stability of **W1**.

There is also a considerable difference in the reaction barrier for **TS1** relative to **W1**; the barrier of the radical anion analogue is 9.6 kcal mol^{-1} lower than the barrier of the neutral radical. To investigate this phenomenon, the reaction path was followed by integrating the intrinsic reaction coordinate *via* a Hessian based predictor–corrector algorithm,[26] as shown in Fig. 13. According to this, H abstraction from the β-carbon has direct involvement of the carboxylate group. This is a charge-driven reaction, which is initiated by the proton shifting from the β-hydroxyl group to the carboxylate moiety, followed by hydrogen abstraction from the β-carbon to the peroxyl group, which can be seen in Fig. 13. Between structures (II) and (III)

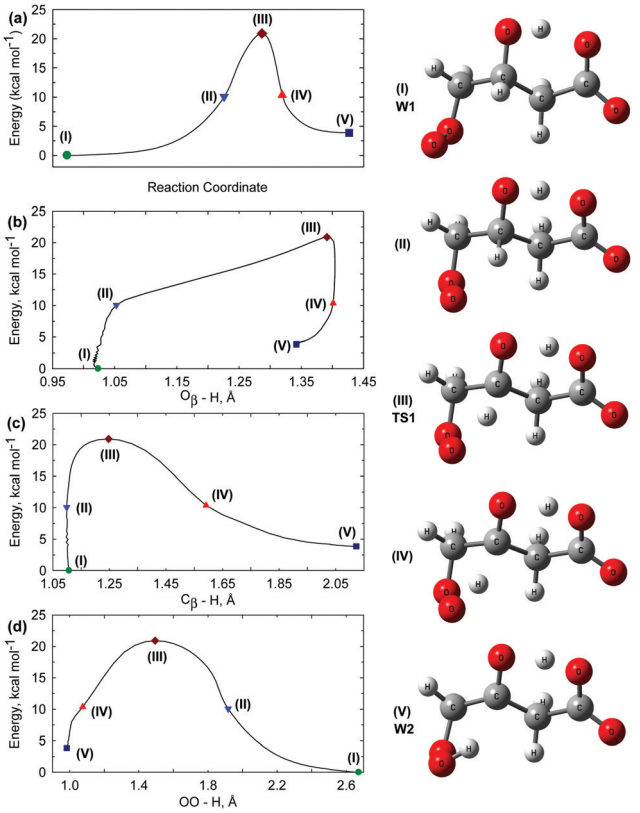

Fig. 13 Intrinsic reaction coordinate scan of **TS1**, including (a) the minimum energy potential of **W1** to **W2** through **TS1**, (b) O_β–H bond length, (c) C_β–H bond length, and (d) OO–H bond length on the minimum energy potential. Geometries at five selected positions along the reaction coordinate are shown at right.

the O–H bond distance elongates consistently, whereas C–H bond fission is initiated later; in the vicinity of the transition state. Post-transition state (III–IV), the carboxylate group remains protonated as the C–H bond fission is completed, only after which (IV–V) the original O–H bond is re-formed. In comparison, in the neutral radical analogue this process is radical-driven as the carboxylic moiety cannot act as a proton acceptor. This leads to the considerable energy difference of **TS1** (9.6 kcal mol^{-1}) between the radical anion and the neutral radical.

Conclusion

A distonic β-hydroxyalkyl radical analogue $^{\bullet}CH_2CH(OH)CH_2C(O)O^-$ has been generated by ion-trap mass spectrometry. Reaction of this radical anion with O_2 proceeds *via* the intermediate β-hydroxyperoxyl radical anion $^{\bullet}O_2CH_2CH(OH)CH_2C(O)O^-$, whose subsequent chemistry is influenced by the additional stability associated with the peculiar electronic configuration, in comparison to its protonated neutral form. Noticeable remote stabilisation of the peroxyl radical anion has been observed, where the SOMO has been assigned as MO 30 and the HOMO (MO 36) is doubly occupied and corresponds to the negatively charged carboxylate moiety. Examination of the other $C_4H_6O_5^{\bullet-}$ isomers revealed that the peroxyl radical anion exhibits different extent of SOMO–HOMO conversion depending on the charge and radical site. As a result, the lowest-energy reaction pathway for the neutral radical involving H abstraction from the β-hydroxyl moiety has been supressed in the radical anion. Instead, facile H abstraction from the β-carbon with direct involvement of the carboxylate group followed by proton transfer to release $^{\bullet}OH$ has become the lowest-energy reaction pathway for the radical anion. The theoretical mechanism is consistent with the experimental findings for the $^{\bullet}CH_2CH(OH)CH_2C(O)O^-$ + O_2 reaction. These results demonstrate that the inclusion of a negatively charged functional group results in the dominant reaction pathway switching from H abstraction from the β-hydroxyl group (**TS13**) to H abstraction from the β-carbon (**TS10**). Importantly, this example shows that – at least in the gas phase – the electronic structure and associated reaction chemistry of peroxyl radicals is modulated by a proximate anion. This may suggest an important interplay exists between radical- and charge-directed mechanisms in the oxidation of biologically important molecules.

Experimental methods

Mass spectrometry

3-Hydroxyglutaric acid was obtained from Sigma Aldrich (Castle Hill, NSW). Isotopically labelled oxygen $^{18}O_2$ (95%) was obtained from Cambridge Isotope Laboratories (Andover, MA). Methanol (HPLC grade) and ammonia solution (28%, AR grade) were obtained from Ajax (Sydney, Australia). Samples were prepared by dissolving a small quantity of 3-hydroxyglutaric acid in a few drops of concentrated aqueous ammonia, followed by dilution of the high pH solution in methanol. Experiments were conducted using a Thermo Fisher Scientific LTQ linear ion-trap mass spectrometer fitted with an IonMax electrospray ionisation source. The diluted analyte was infused by electrospray ionisation at a rate of 3–5 μL min^{-1}. Typical electrospray source conditions employed a spray voltage of 3.2 kV and a capillary temperature of 100 °C, with the arbitrary units of sheath gas, aux gas and sweep gas set to be 15–20, 0–5 and 0 respectively. The mass spectrometer used here has been modified to enable both laser-induced photodissociation and ion–molecule experiments, details of which have been reported previously.[16,19] An overview of the modifications is outlined below.

Laser-Induced photodissociation

An aperture and CF flange was milled into the back-plate of the linear ion-trap and a 2.75″ quartz window was installed to allow transmission and overlap of a 266 nm laser pulse generated by a Nd:YAG laser (Continuum Minilite II, Santa Clara; pulse-energy: *ca.* 30 mJ cm^{-2}) with an isolated ion cloud. In each mass spectrometry cycle, a transistor–transistor logic (TTL) pulse is generated by the mass spectrometer during a selected MS^n activation stage that triggers the flash lamp of the laser. The collision energy of the selected MS^n activation stage is set to 0 (arbitrary units) such that all products generated arise from the incident laser pulse and not collisional excitation. All photodissociation experiments

were conducted using 266 nm radiation (*ca.* 1 mJ per pulse, 10 Hz repetition rate) with only a single laser pulse (pulse width approximately 7 ns) irradiating the selected ions per mass spectrum cycle.

Ion–molecule reactions

Residual molecular oxygen ($^{16}O_2$) is present in the ion-trap region of the mass spectrometer due to transmission from the atmosphere *via* the electrospray ionisation source. The concentration of oxygen is estimated from a calibration reaction of 3-carboxylatoadamantyl + O_2.[16] A higher concentration of oxygen was obtained by replacing the standard UHP helium buffer gas with a 770 ± 45 ppm O_2 in helium premix (BOC, Australia). For the experiments involving ^{18}O-labelled dioxygen, a flow of $^{18}O_2$ (<0.020 mL min^{-1}) is entrained *via* a septum inlet into a flow of ultra-high purity helium (3–5 psi), which is adjusted with a variable leak valve to obtain an ion-trap pressure of approximately 2.5 mTorr (total flow was about 2.1 mL min^{-1}). In these experiments adventitious $^{16}O_2$ is still present.

Reaction rates for the oxidation of distonic radical ions were obtained by recording a decay plot of the precursor radical ion count with increasing isolation times, where reaction times were set at 30–10 000 ms *via* the instrument activation time parameter, with the activation energy set to zero (arbitrary units). Using eqn (1), a single exponential is used to fit the decay curve to obtain the pseudo-first order rate constant (k_1). The true second-order rate constant (k_2) is then calculated from the measured pseudo-first order rate constant (k_1) using the estimated oxygen concentration as shown in eqn (2). Finally, by calculating the collision rate coefficient (k_{coll}) using trajectory collision rate theory, the reaction efficiency (ϕ) can be determined using eqn (3).

$$\frac{[R]_t}{[R]_0} = \exp(-k_1 t) \quad (1)$$

$$k_2 = \frac{k_1}{[O_2]} \quad (2)$$

$$\phi = \frac{k_2}{k_{coll}} \quad (3)$$

Statistical errors in these rate measurements are typically $2\sigma <$ 10%, where σ is the standard deviation of the least-squared fit to the pseudo first-order decay. Systematic errors arise primarily from uncertainty in the ion-trap pressure and temperature[16] (assumed here to be 2.5 mTorr and 307 ± 1 K) and product ions of $m/z < 50$ formed in the reaction that are detected with poor efficiency. Overall, reactions measured on this instrument using an oxygen concentration estimated from the calibration reaction described above are expected to have a relative error of less than 10%, while an error of 50% is ascribed to the absolute second-order rate constant.

Electronic structure calculations

Calculations were performed using Gaussian 09.[27] Stationary points on the $C_4H_6O_5^{\bullet -}$ surface (for the *R* enantiomer) were located using the M06-2X[28] and B3LYP[29,30] density functionals and the 6-31G(2df,p) basis set. All reported calculations refer to the lowest energy conformation of each stationary point. Minima and transition states were confirmed to have zero and one imaginary frequency, respectively. Additional single point energy calculations were performed using the M06-2X/6-31G(2df,p) geometries with the larger aug-cc-pVTZ basis set, and these calculations returned spin-squared operators within a few percent of the expected values, except for TS9 (12%), which may be impacted by spin contamination. Structures optimised by the B3LYP model chemistry were utilised in high level energy calculations using the G4 composite method.[31] These methods have been widely employed for open-shell species, and the expected mean error of the two model chemistries is 1–2 kcal mol^{-1}.[28,31] Coordinates, vibrational frequencies and moments of inertia of the stationary points at M06-2X/6-31G(2df,p) level of theory are provided in the ESI.†

Unrestricted density functional calculations were performed to determine the electronic arrangement and molecular orbital configurations of the distonic radical anions using M06-2X/6-31G(2df,p) geometries with the aug-cc-pVTZ basis set. Using similar procedures as described in the literature,[20] the energy and shape of the α-spin and β-spin electron orbitals were used to pair electrons into the same DOMO. A SOMO was assigned when the energy and structure of an occupied orbital with an α-spin electron could not be suitably matched with any of the occupied orbitals with a β-spin counterpart. Plots of molecular orbitals and spin density were generated using GaussView 5.0.[32]

Conflicts of interest

There are no conflicts to declare.

Acknowledgements

Support by the Australian Research Council under the Discovery Project Scheme (DP170101596) is gratefully acknowledged.

References

1 A. D. McNaught and A. Wilkinson, *Compendium of Chemical Terminology*, Blackwell Scientific Publications, Oxford, 1997.
2 T. Sugawara, H. Komatsu and K. Suzuki, *Chem. Soc. Rev.*, 2011, **40**, 3105.
3 T. Kusamoto, S. Kume and H. Nishihara, *J. Am. Chem. Soc.*, 2008, **130**, 13844.
4 Y. Kobayashi, M. Yoshioka, K. Saigo, D. Hashizume and T. Ogura, *J. Am. Chem. Soc.*, 2009, **131**, 9995.
5 G. Gryn'ova and M. L. Coote, *J. Am. Chem. Soc.*, 2013, **135**, 15392.
6 M. L. Gross and F. W. McLafferty, *J. Am. Chem. Soc.*, 1971, **93**, 1267.
7 M. L. Gross, *J. Am. Chem. Soc.*, 1972, **94**, 3744.
8 B. F. Yates, W. J. Bouma and L. Radom, *J. Am. Chem. Soc.*, 1984, **106**, 5805.

9 K. M. Stirk, L. K. M. Kiminkinen and H. I. Kenttamaa, *Chem. Rev.*, 1992, **92**, 1649–1665.
10 P. E. Williams, B. J. Jankiewicz, L. Yang and H. I. Kenttamaa, *Chem. Rev.*, 2013, **113**, 6949.
11 S. So, B. B. Kirk, A. J. Trevitt, U. Wille, S. J. Blanksby and G. da Silva, *Phys. Chem. Chem. Phys.*, 2014, **16**, 24954.
12 M. B. Prendergast, P. A. Cooper, B. B. Kirk, G. da Silva, S. J. Blanksby and A. J. Trevitt, *Phys. Chem. Chem. Phys.*, 2013, **15**, 20577.
13 A. Kumar and M. D. Sevilla, *J. Phys. Chem. B*, 2014, **118**, 5453.
14 P. Franchi, E. Mezzina and M. Lucarini, *J. Am. Chem. Soc.*, 2014, **136**, 1250.
15 B. B. Kirk, D. G. Harman and S. J. Blanksby, *J. Phys. Chem. A*, 2009, **114**, 1446.
16 D. G. Harman and S. J. Blanksby, *Org. Biomol. Chem.*, 2007, **5**, 3495.
17 G. N. Khairallah, R. A. J. O'Hair and U. Wille, *J. Phys. Chem. A*, 2014, **118**, 3295.
18 R. K. Sinha, P. Maître, S. Piccirillo, B. Chiavarino, M. E. Crestoni and S. Fornarini, *Phys. Chem. Chem. Phys.*, 2010, **12**, 9794.
19 T. Ly, B. B. Kirk, P. I. Hettiarachchi, B. L. Poad, A. J. Trevitt, G. da Silva and S. J. Blanksby, *Phys. Chem. Chem. Phys.*, 2011, **13**, 16314.
20 G. Gryn'ova, D. L. Marshall, S. J. Blanksby and M. L. Coote, *Nat. Chem.*, 2013, **5**, 474.
21 J. E. McClellan, J. P. Murphy, J. J. Mulholland and R. A. Yost, *Anal. Chem.*, 2002, **74**, 402.
22 I. Hermans, J.-F. Müller, T. L. Nguyen, P. A. Jacobs and J. Peeters, *J. Phys. Chem. A*, 2005, **109**, 4303.
23 G. da Silva, J. W. Bozzelli, L. Liang and J. T. Farrell, *J. Phys. Chem. A*, 2009, **113**, 8923.
24 G. da Silva and J. W. Bozzelli, *Chem. Phys. Lett.*, 2009, **483**, 25.
25 P. E. Williams, D. L. Marshall, B. L. J. Poad, V. R. Narreddula, B. B. Kirk, A. J. Trevitt and S. J. Blanksby, *J. Am. Soc. Mass Spectrom.*, 2018, **29**, 1848.
26 H. P. Hratchian and H. B. Schlegel, *J. Chem. Phys.*, 2004, **120**, 9918.
27 M. J. Frisch, *et al.*, *Gaussian 09, Revision B.01*, Gaussian Inc., Wallingford CT, 2016.
28 Y. Zhao and D. G. Truhlar, *Theor. Chem. Acc.*, 2008, **120**, 215.
29 P. Stephens, F. Devlin, C. Chabalowski and M. J. Frisch, *J. Phys. Chem.*, 1994, **98**, 11623.
30 A. D. Becke, *J. Chem. Phys.*, 1993, **98**, 1372.
31 L. A. Curtiss, P. C. Redfern and K. Raghavachari, *J. Chem. Phys.*, 2007, **126**, 084108.
32 R. Dennington, T. A. Keith and J. M. Millam, *GaussView, Version 5*, Semichem Inc., Shawnee Mission, KS, 2009.